frontiers | Frontiers in Earth Science

TYPE Original Research
PUBLISHED 21 April 2023
DOI 10.3389/feart.2023.1135335

OPEN ACCESS

EDITED BY
Rafael Almeida,
San Diego State University, United States

REVIEWED BY
Yan Qiu,
Guangzhou Marine Geological Survey, China
Wenhuan Zhan,
South China Sea Institute of Oceanology (CAS), China

*CORRESPONDENCE
Cong Chen,
chenc66@mail.sysu.edu.cn

†These authors have contributed equally to this work

SPECIALTY SECTION
This article was submitted to Quaternary Science, Geomorphology and Paleoenvironment, a section of the journal Frontiers in Earth Science

RECEIVED 31 December 2022
ACCEPTED 05 April 2023
PUBLISHED 21 April 2023

CITATION
Chen Z, Wang W, Huang P, Tang Y, Wang J, Zeng Q and Chen C (2023), Soft-sediment deformation structures of mottled clay in Huizhou Quaternary basin, coastal South China. *Front. Earth Sci.* 11:1135335. doi: 10.3389/feart.2023.1135335

Soft-sediment deformation structures of mottled clay in Huizhou Quaternary basin, coastal South China

Zhen Chen[1,2†], Wen Wang[3†], Ping Huang[2], Yongjie Tang[1], Jing Wang[4], Qiang Zeng[2] and Cong Chen[1*]

[1]School of Earth Sciences and Engineering, Sun Yat-sen University, Zhuhai, China, [2]GDZD Institute on Deep-Earth Sciences, Guangzhou, China, [3]Nonferrous Metals Geological Bureau of Guangdong Province 935 Battalion, Huizhou, China, [4]Museum and History Museum of Sun Yat-sen University, Guangzhou, China

Tectonically induced liquefaction and the resulting soft-sediment deformation structure (SSDS) can provide useful information on paleo-earthquakes, which is vital for the assessment of geohazard susceptibility in tectonically active regions. In this study, we combined sedimentary and chronological methods to the reveal detailed characteristics of the mottled clay in the Huizhou Quaternary Basin. The dating results suggest that mottled clay usually developed during the late Pleistocene, overlying the fluvial deposit or embedding homogeneous aeolian yellow silt. Mottled clay has a typical bimodal frequency distribution with modal sizes at 5 and 80–90 μm, which are identical to those of the yellow silt and the underlying fluvial sand, respectively. Micro-X-ray fluorescence mapping revealed high concentrations of Fe and Si in the red and white fraction, respectively. In addition, the red fraction of mottled clay has a high hematite content, similar to loess-like yellow silt, whereas the white fraction and the underlying fluvial sediments are dominated by goethite. This sedimentary evidence together suggests that the mottled clay could be an admixture of aeolian yellow silt and the underlying fluvial sand. Furthermore, diverse deformed structures (e.g., fragmented structures, sand veins, sand dykes and flame structures) were observed in mottled clay. Therefore, we suggest that the mottled clay structure in the Huizhou Basin is a product of liquefaction-induced SSDS. Tectonic activity was considered to have triggered the liquefaction and SSDS, which is supported by the close spatial relationship between the mottled clay and regional faults. We propose that the SSDS of mottled clay could be a potential indicator of paleo-earthquakes in the coastal Quaternary basins of the northern South China Sea.

KEYWORDS

soft-sediment deformation, mottled clay, tectonic activity, late Pleistoncene, Huizhou basin, South China

1 Introduction

Tectonic-induced liquefaction and resulting soft-sediment deformation structure (SSDS) that was preserved in the geological record, are commonly used to derive information (e.g., intensity and recurrence intervals) of paleo-earthquake, and are thus vital for the assessment of geohazard susceptibility in tectonically active regions (Allen, 1986; Deev et al., 2009; Qiao et al.,

2017; Liang et al., 2018; Tuttle et al., 2019; Üner et al., 2019). For example, a compilation of historical earthquakes that occurred during the last millennium and the related liquefaction in Italy permitted the establishment of an empirical relationship between the magnitude and distance of liquefaction (Galli, 2000). An integrated method was applied to provide information on the seismic shaking intensity recorded in lacustrine sediments at sites where it was difficult to conduct research by excavating trenches owing to their rough topography, strong erosion, or the absence of co-seismic ruptures (Zhong et al., 2022). In particular, paleo-earthquakes in the late Quaternary are actively researched because their potential risk to contemporary urban growth and safety in habitations, which have been successfully identified, for instance, in Ecuador (Hibsch et al., 1997), Kyrgyzstan (Gladkov et al., 2016), and Brazil (Rossetti et al., 2017), mostly based on liquefaction and SSDS features in the deposit profiles. However, in addition to earthquakes, liquefaction-induced SSDS can also be triggered by other factors, such as water waves, rapid sediment accumulation, groundwater movement, ice-wedges, and meteorites (Owen and Moretti, 2011; Su et al., 2022). Therefore, correctly determining the trigger for liquefaction-induced SSDS is fundamental for interpreting information on paleo-earthquake. A methodology and criteria for analyzing SSDS and distinguishing the triggers have been proposed, involving sedimentological, paleoenvironmental and tectonic contexts (Owen and Moretti, 2011).

In the coastal region of the northern South China Sea (SCS), there are many Quaternary basins, such as the Pearl River Delta (PRD), Lianjiang Plains, Hanjiang Delta and Fujian coastal basins, the emergence of which is generally related to the regional neo-tectonic activity (Chen et al., 2002; Yao et al., 2013). Previous studies have also revealed geological evidence of late Quaternary fault activity (e.g., Song et al., 2001; Tang et al., 2011). For example, a sedimentary layer younger than 23 ka was cut off by a normal fault with a fault-throw of 53 cm at the Xilingang Site in the PRD (Tang et al., 2011). Several historical earthquake events are also documented (Wei et al., 2000). This implies that the PRD with a dense population and economic activity is tectonically active. Moreover, most Quaternary basins are filled with several to dozens of meters of loose, water-saturated silt and sand, consisting mainly of fluvial, marine and aeolian sediments (Wang et al., 2018a; Tang et al., 2018). Tectonic and sedimentary features generally favor the development of liquefaction (Owen and Moretti, 2011). However, tectonic activity-induced liquefaction and related SSDS in the PRD remain poorly understood. Mottled clay, which exhibits a mixed yellow, red and white color, broadly developed in these coastal Quaternary basins and is primary regarded as a weathering product of the underlying fluvial/marine sediments (Huang, 1982; Li et al., 1984). Later, Wang et al. (2018b) suggested an aeolian origin of the mottled clay rather than a weathering product based on sedimentary and geochemical analyses, and proposed that the mottled structure was formed by post-sedimentary modification of oxidation. Recently, we studied a series of drilling cores derived from the Huizhou Basin (HZB) in the eastern PRD and found diverse deformed structures in the mottled clay sediments, implying a potential liquefaction origin of the mottled structure.

In this study, we combined sedimentary and chronological methods, including lithological feature, grain size analysis, micro-X-ray fluorescence (μ-XRF) scanning, diffuse reflectance spectroscopy (DRS) analysis, and accelerator mass spectrometry radiocarbon dating (AMS ^{14}C), to reveal detailed characteristics of mottled clay in the drilling cores derived from the HZB. We further discuss the origin of the mottled structures, which are possibly liquefaction-induced SSDS triggered by regional neo-tectonic activity during the late Pleistocene.

2 Geological settings

The Pearl River, one of the longest watercourses in southern China, includes three major tributaries (i.e., the Xijiang River, Beijiang River and Dongjiang River), and its delta (the PRD) is the largest Quaternary plain in the coastal northern SCS (Figure 1A). The HZB situated in the eastern PRD is an alluvial basin of the middle Dongjiang River, ranging from 114°20' to 114°40' E and 22°50' to 23°10' N. The evolution of the Huizhou Basin was mostly controlled by the SW-NE and NW-SE faults, that is, the Huizhou Fault to the west, Lianghua Fault to the east, the Zijin-Boluo Fault and Tonghu Fault to the north, and the Lianhuashan Fault to the south (Figure 1B) (Li et al., 2020, 2021). The Zijin-Boluo and Tonghu faults belong to the same regional fault zone, with a length of approximately 20 km, striking NE, inclining SE and dipping 40°–60°. The Lianhuashan Fault is part of the Wuhua-Shenzhen Fault zone, striking NE and inclining NW. The Huizhou Fault is approximately 20 km long, striking NW, inclining NE and dipping 65°–75°. All five faults are normal faults (BGMRGP, 1988), and are considered as being active. The bedrock of the HZB consist mainly of Jurassic and Cretaceous igneous rock and sandstone, which have an unconformity contact with the overlying unconsolidated late Quaternary sediments. At present, the HZB experiences a subtropical monsoonal climate, with a mean annual temperature of 21.9°C, summer temperature of 27.9°C and winter temperature of 14.5°C, respectively, between 1954 and 2006 AD (Li et al., 2008).

3 Material and methods

3.1 Drilling cores

In this study, 12 cores (Table 1) were drilled in the HZB during April-May 2022 to reveal the features of Quaternary sediments in the basin. Combined with three published drilling cores, the lithological chart shows that the Quaternary sediments are generally approximately 15–25 m thick, and the overall succession can be divided into three units from the bottom to the top based on the lithology as follows (Figure 2): 1) Unit I, Q_3^a fluvial sediment; the lithology is grayish white to yellow gravel sand, sand or clay sand, underlain by weathered pre-Cenozoic bedrock. The thickness of this unit is generally larger than 10 m. 2) Unit II, Q_3^b aeolian sediment, mostly consists of loess-like silt, with occasional mottled clay. The thickness of this unit varies in the basin, mostly between 2 and 10 m. 3) Unit III, Q_4 fluvial or marsh sediments; it mainly consists of gray to yellow coarse to fine sand, silt and clay. The organic carbon content of this unit is generally higher than that of Unit I. In particular, a mottled clay structure with 1–5 m thick was found in seven of the 12 drilling cores in the HZB. The mottled clay exhibits a mixed yellow, red and grey-white color, and the bright clay generally shows vein- and/or

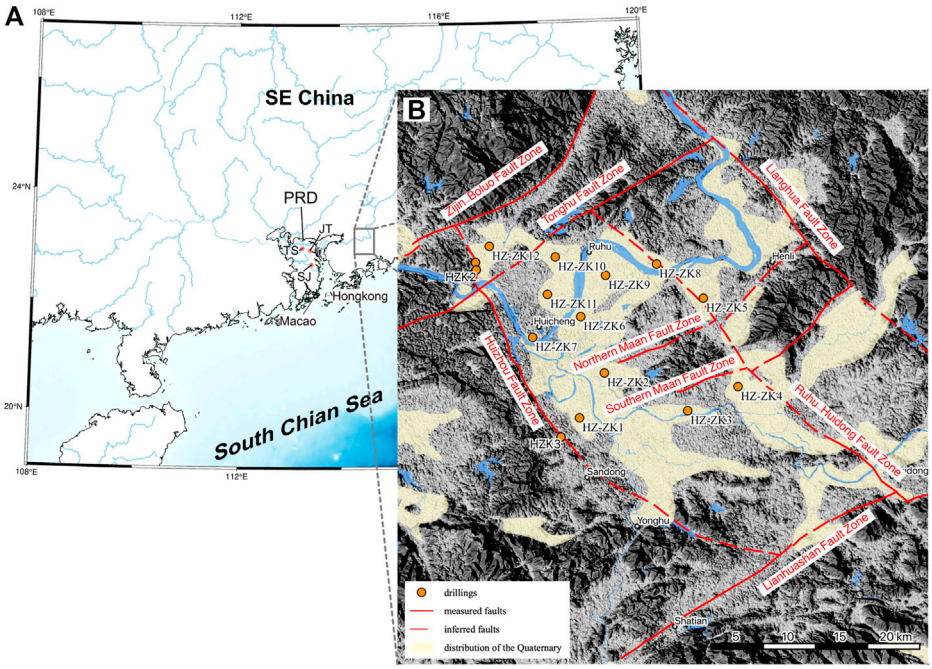

FIGURE 1
Location and tectonic landform map of the Huizhou Basin. **(A)** The location of the Pearl River Delta PRD and the Huizhou Basin. JT, SJ and TS were the sampling locations of Wang et al. (2018b). **(B)** Distribution of the Quaternary sediment, regional basement faults and the locations of the drilling cores.

TABLE 1 Locations of the drilling cores in the Huizhou Basin.

Core ID	Longitude (E)	Latitude (N)	Elevation (m)	Mottled clay
HZ-ZK01	114° 27′ 02.3448″	23° 01′ 51.4574″	11.7	No
HZ-ZK02	114° 28′ 19.3890″	23° 04′ 10.9721″	11.6	No
HZ-ZK03	114° 32′ 37.8219″	23° 02′ 13.6413″	15.5	No
HZ-ZK04	114° 35′ 13.9168″	23° 03′ 28.5875″	15.9	Yes
HZ-ZK05	114° 33′ 26.3536″	23° 08′ 03.1127″	15.0	Yes
HZ-ZK06	114° 27′ 06.0229″	23° 07′ 05.7405″	11.1	Yes
HZ-ZK07	114° 24′ 36.9448″	23° 06′ 01.1982″	14.2	No
HZ-ZK08	114° 31′ 01.4063″	23° 09′ 48.9913″	13.2	No
HZ-ZK09	114° 28′ 23.1944″	23° 09′ 13.6555″	10.7	Yes
HZ-ZK10	114° 25′ 47.2292″	23° 10′ 10.8851″	12.0	Yes
HZ-ZK11	114° 25′ 22.8159″	23° 08′ 14.7721″	11.7	Yes
HZ-ZK12	114° 22’ 22.2858″	23° 10′ 43.8220″	10.7	Yes

flame-like vertical structures intruding into yellow/red sediments (Figure 3B). The deformation features were clearly distinguished from the underlying loess-like silt or fluvial sand deposits (Figure 3). The normal aeolian sediment is homogeneous in color and grain size (Figure 3A), and fluvial sand deposits present pronounced horizontal features (e.g., laminae).

3.2 AMS ^{14}C dating

To constrain the age of the Quaternary stratigraphy in the HZB, we collected ten samples from the drilling cores for AMS ^{14}C dating. Bulk organic sediment samples were pretreated using the standard acid-base-acid (ABA) method and analyzed at the

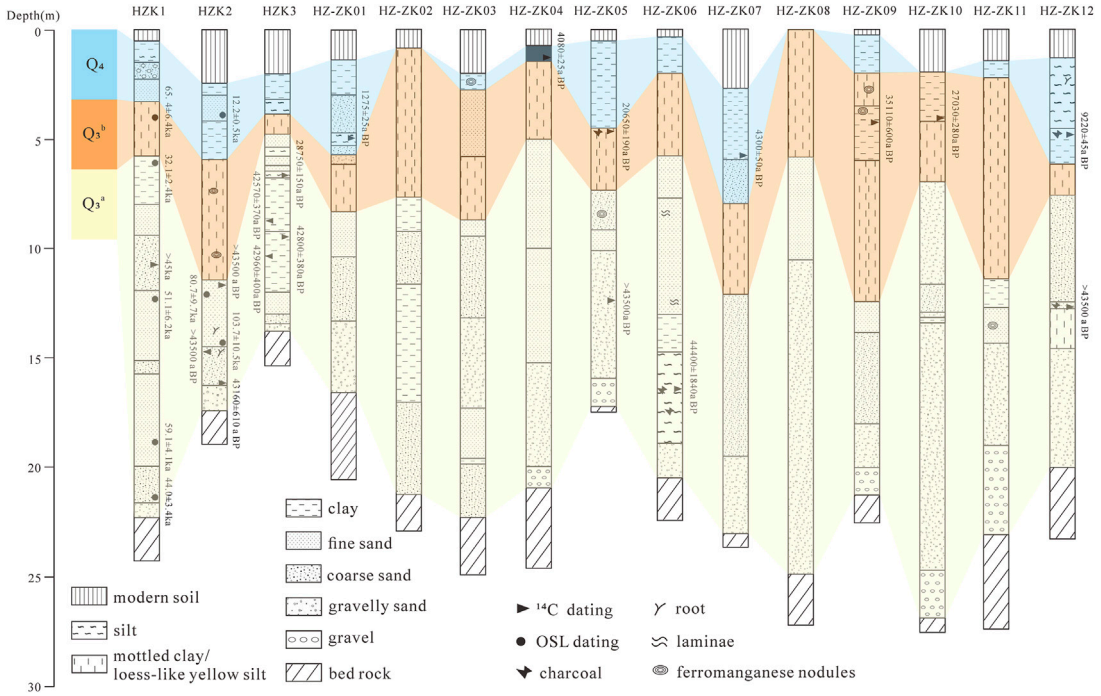

FIGURE 2
Comparison chart of the drilling cores in the Huizhou Basin. Cores HZK1-3 are according to Li et al. (2021). AMS ^{14}C and OSL dating results are also indicated.

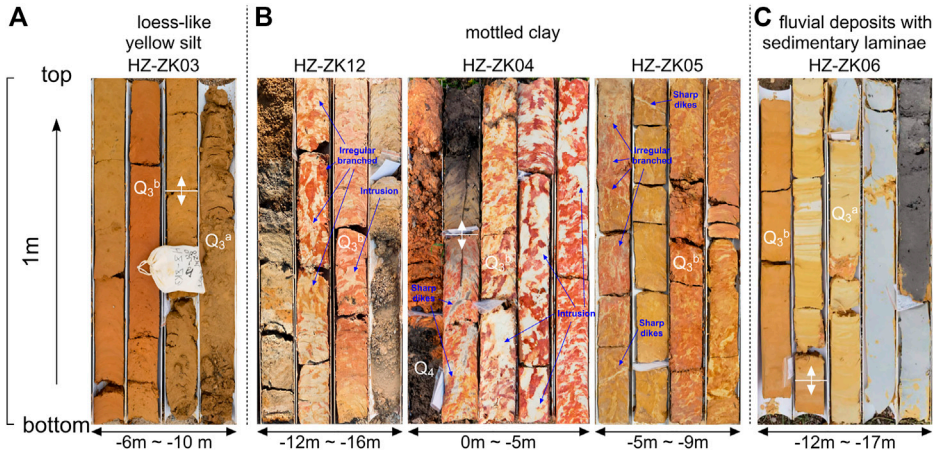

FIGURE 3
Photograph of different lithological layers in the Huizhou Basin. **(A)** Homogeneous loess-like yellow silt. **(B)** Mottled clay, exhibiting a yellow, red and grey-white mixed color and vertical structure. **(C)** Fluvial sand deposit with horizontal features.

Qingdao National Laboratory for Marine Science and Technology, China. The dates were then calibrated to calendar years (i.e., cal BP) using the IntCal20 Data Sets (Reimer et al., 2020) (Table 2). Additionally, the optically stimulated luminescence (OSL) dates provided in a previous study (Li et al., 2021) were combined to constrain the age of the lower fluvial deposit (Figure 2), which is generally beyond the dating limit of the AMS ^{14}C method.

3.3 μ-XRF, DRS and grain size analysis

In this study, we conducted μ-XRF and DRS analysis to reveal detailed geochemical element and iron oxide features of mottled clay structure in the HZB. Three thin sections of mottled clay structure (10 cm in diameter and dozens of centimeters in length) (Table 3) were collected for μ-XRF scanning, using an M4 Plus Micro Area X-Ray Fluorescence Analyzer at Guangzhou Tuoyan Analytical Technology Co. Ltd. The

TABLE 2 AMS^{14}C dating results of the late Pleistocene sediments in the Huizhou Basin.

Sample no.	Depth (m)	Material	Radiocarbon age (a BP)	Calibrated age (2σ, cal a BP)
HZ-ZK01-^{14}C-01	4.81	organic sediment	1275 ± 25	1131–1284
HZ-ZK04-^{14}C-01	1.25	organic sediment	4080 ± 25	4444–4478
HZ-ZK05-^{14}C-01	4.85	charcoal	20650 ± 190	24254–25303
HZ-ZK05-^{14}C-02	12.35	charcoal	-	-
HZ-ZK06-^{14}C-01	16.44	charcoal	44400 ± 1840	43429–51403
HZ-ZK07-^{14}C-01	5.71	charcoal	4300 ± 50	4655–5038
HZ-ZK09-^{14}C-01	4.30	organic sediment	35110 ± 600	39108–41369
HZ-ZK10-^{14}C-01	4.10	organic sediment	27030 ± 280	30474–31692
HZ-ZK12-^{14}C-04	4.90	organic sediment	9220 ± 45	10249–10504
HZ-ZK12-^{14}C-02	12.70	charcoal	-	-

TABLE 3 Sampling information and analysis methods.

Sample ID	Drilling core	Depth (m)	Lithological	Method
XRF-01	HZ-ZK04	3.30–3.60	mottled clay	μ-XRF
XRF-02	HZ-ZK05	6.05–6.20	mottled clay	μ-XRF
XRF-03	HZ-ZK12	13.30–13.35	mottled clay	μ-XRF
UV-01	HZ-ZK03	7.50	loess-like yellow silt	DRS
UV-02	HZ-ZK12	13.36	red fraction of mottled clay	DRS
UV-03	HZ-ZK12	13.40	white fraction of mottled clay	DRS
UV-04	HZ-ZK06	13.50	fluvial sand	DRS
GS-01	HZ-ZK06	2.70	loess-like yellow silt	grain size
GS-02	HZ-ZK06	3.50	mottled clay	grain size
GS-03	HZ-ZK06	4.50	mottled clay	grain size
GS-04	HZ-ZK06	5.50	mottled clay	grain size
GS-05	HZ-ZK06	8.50	loess-like yellow silt	grain size
GS-06	HZ-ZK06	13.80	fluvial sand	grain size
GS-07	HZ-ZK06	15.80	fluvial sand	grain size
GS-08	HZ-ZK06	17.80	fluvial sand	grain size
GS-09	HZ-ZK06	18.40	fluvial sand	grain size

instrument is equipped with a 20 μm diameter polycapillary X-ray lens and two X-Flash silicon drift detectors and operated at a voltage of 50 kV and a current of 300 μA. The scanning was carried out at a 20 μm spot size, 5 ms acquisition time and 35 μm points distance. Original data were processed using M4 tornado software to analyze the spectral peak information, and derive the element surface distribution map.

Four samples with different lithologies (Table 3) were ground in an agate mortar and passed through a 200-mesh sieve prior to DRS analysis. In particular, the red and white fractions of mottled clay were separated into two separate samples. DRS analysis was conducted using a Perkin Elmer (U.K.) ultraviolet-visible near-infrared spectrophotometer with a wavelength range of 175–3,300 nm at the Instrumental Analysis & Research Center of Sun Yat-sen University. Data for the visible light range of 400–700 nm were collected at 1 nm intervals and used as the first-order derivative of the peak height mapping.

Furthermore, we collected samples from different lithological layers of core HZ-ZK06 for grain size analysis. The grain size was determined using a Malvern (U.K.) Mastersizer 2000 laser particle size instrument (measurement error <2%). Prior to measurement, the samples were pretreated with 10% H_2O_2 and 10% HCl to remove organic matter and carbonates, respectively. Then samples were washed with distilled water, sieved through a 1,000 μm mesh, and dispersed with 0.05 mol/L sodium hexametaphosphate $(NaPO_3)_6$ solution. Before the analysis, the samples were placed in an ultrasonic vibrator for 20 min.

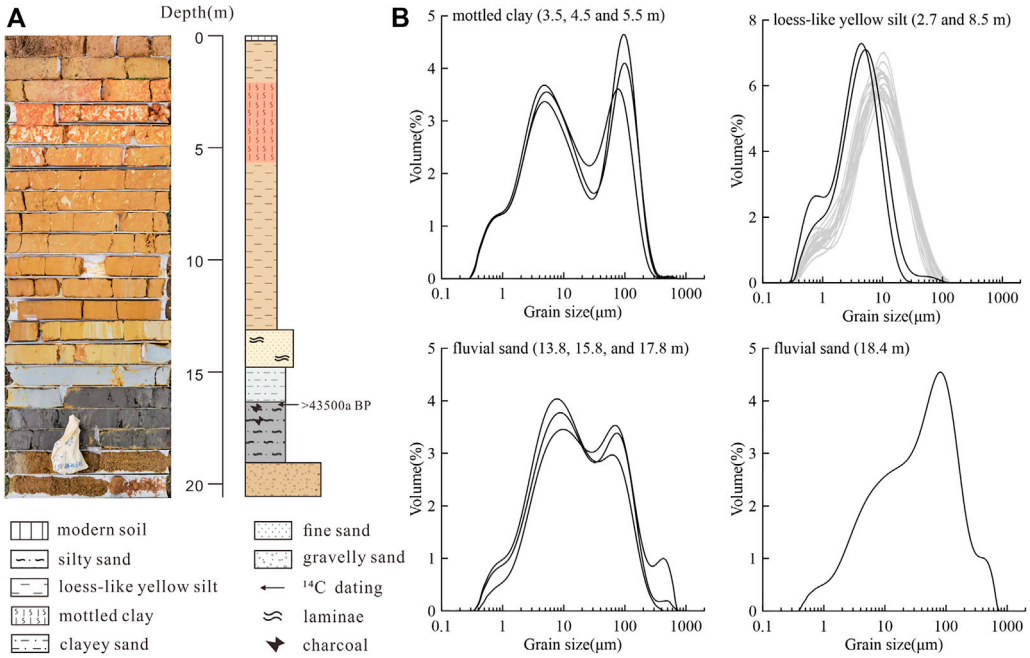

FIGURE 4
Lithology and grain size distribution of core HZ-ZK06. **(A)** Photography and lithology of core HZ-ZK06. **(B)** Grain size frequency distribution of different lithological layers from core HZ-ZK06. The frequency distribution of loess-like yellow silt in the Pearl River Delta is also shown (grey lines) (Wang et al., 2018b).

4 Results

4.1 Dating results

The results suggest that the unconsolidated sediment in the HZB has mostly developed since the late Pleistocene, directly overlying the weathered pre-Cenozoic bedrock. The radiocarbon dating results of the samples from HZ-ZK01, HZ-ZK04, HZ-ZK07, and ZH-ZK12 suggest that the uppermost Unit III (fluvial or marsh sediments) was mostly deposited during the Holocene (Table 2). The ages of the samples from Unit II (aeolian sediment) ranged between 20 and 35 ka BP, which is consistent with the ages of the yellow silt in the PRD. Wang et al. (2018a, b) demonstrated that the aeolian deposits found in most Quaternary basins of Southeast China developed during the Last Glacial period and were predominantly deposited during the Last Glacial Maximum (LGM). However, the ages of the underlying fluvial sediments (Unit I) exceeded the beyond the he dating limit of the AMS ^{14}C method. A previous study using the OSL dating method (Li et al., 2021) suggests that Unit I could be older than 103 ± 10.5 ka (Figure 2).

4.2 Grain size characteristics

Grain size analysis is one of the most popular methods used for the analysis of sediments and helps determine the transport agents and sedimentary environment (Xu et al., 1992). The grain size distribution characteristics of the samples from core HZ-ZK06 generally became finer from the bottom to the top (Figure 4B). Specifically, the frequency distribution curves of the fluvial deposits have a unimodal or multimodal form biased towards the coarse-grain end. The primary modal size of the lower fluvial sample (18.4 m) was around 85 μm, while those of the upper fluvial samples (13.8, 15.8, and 17.8 m) were around 75 and 9 μm, respectively. The yellow silt samples (2.7 and 8.5 m) present a uniform unimodal distribution with a fine tail and sharp kurtosis. The modal size of yellow silt is about 5 μm. The curves of yellow silt in the HZB decreased abruptly at the coarse-grained end and more gradually at the fine-grained end, similar to those of the loess-like yellow silt in the PRD (Figure 4B) and typical Chinese loess (Wang et al., 2018a). However, the modal size of yellow silt in the HZB is finer than those in the PRD (~16 μm), indicating wind sorting and decreasing transporting capacity. Nevertheless, our results suggest that the yellow silt in the HZB shares a common sedimentary type (aeolian) with loess-like yellow silt in the PRD and typical loess in China.

The mottled clay in core HZ-ZK06 occurred as an interbed within a thick layer of homogeneous yellow silt (Figure 4A), showing a deformation structure. The frequency distribution curves of the samples have a typical bimodal distribution, with a primary modal size of 80–90 μm and a secondary modal size of about 5 μm. Interestingly, the two distinct modal sizes were identical to those of the yellow silt and underlying fluvial sand, respectively. The finer part (<20 μm) of the curves is also similar with the curves of yellow silt. This implies that the mottled clay may be an admixture of fluvial sand and yellow silt.

4.3 μ-XRF element mapping

μ-XRF is a non-destructive method offering excellent spatial resolution and high sensitivity for small geochemical element

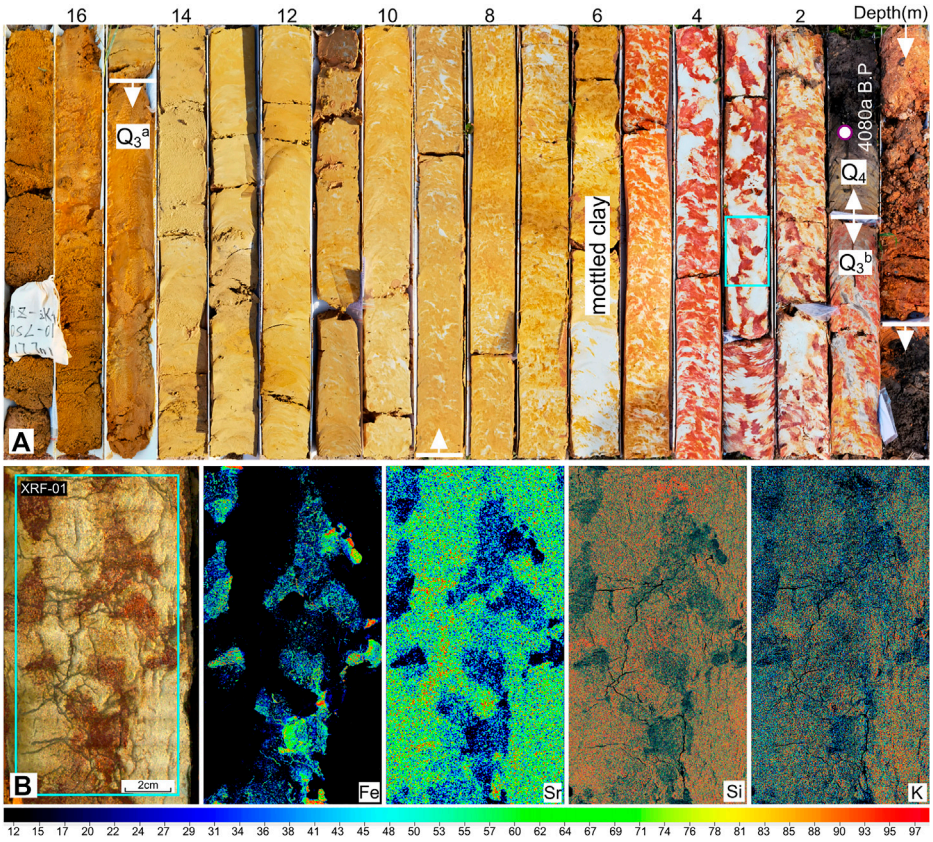

FIGURE 5
Photograph **(A)** and μ-XRF element mapping of mottled clay structure **(B)** of core HZ-ZK04. The mottled clay shows a fragmented structure in the spatial distribution of elements.

concentrations (Hoehnel et al., 2018). In this study, three thin sections of mottled clay showed a heterogeneous spatial distribution of geochemical elements. Generally, the red/yellow fraction of the mottled clay had high concentrations of Fe and Cr, whereas the gray/white fraction had high Si, Al and K concentrations (Figure 5, Figure 6, Figure 7). In particular, the visual structures of samples can be characterized by the varying concentrations of Fe, because the redness of the sediment is dominantly controlled by the type and concentration of iron oxides (Sun et al., 2011). Moreover, the core HZ-ZK04 sample showed a fragmented structure in the spatial distribution of elements (Figure 5B). In core HZ-ZK05, a small white sand vein was characterized by extremely low Fe concentrations, intruding into yellow silt with high Fe concentrations (Figure 6B).

4.4 DRS characteristics

Discriminating iron oxides is of great environmental significance; for example, they are indicators of the sedimentary environment (Zhang et al., 2009). In the subtropical region, hematite and goethite are the two main iron oxide minerals (Wang et al., 2018b), the contents of which in the sediment can be obtained from the DRS first-order derivative curves. The characteristic peak of hematite is typically observed at a wavelength of 565 nm, whereas goethite has two characteristic peaks at 535 and 435 nm (Deaton and Balsam, 1991; Ji et al., 2002). In general, goethite tends to be enriched in wet environments, whereas large amounts of hematite reflect dry environments (Cornell and Schwertmann, 2003; Balsam et al., 2004).

In this study, two peaks at wavelengths of 565 and 435 nm were presented in the loess-like yellow silt (UV-01) and the red fraction of mottled clay (UV-02) samples (Figure 8). The peak at 565 nm is substantially greater than that at 435 nm, which indicates that hematite predominates over goethite in the loess-like yellow silt and the red fraction of mottled clay. Due to overall low iron content as revealed by μ-XRF analysis (Figures 5–7), the DRS curve of the white fraction of mottled clay (UV-03) is relatively flat, and three peaks could be discerned at 435, 505 and 555 nm, respectively (Figure 8). The hematite peak at 565 nm is usually offset to 555 or 575 nm after being affacted by the Fe content, and the characteristic peak of goethite at 535 nm is often biased toward 505 nm (Deaton and Balsam, 1991; Ji et al., 2002). Therefore, the white fraction of the mottled clay contained both goethite and hematite, with the former being higher than the latter. The DRS curve of the fluvial sand (UV-04) shows two peaks at 435 and 505 nm, indicating the predominance of goethite. Overall, the curves of the loess-like yellow silt and the red fraction of mottled clay (UV-01 and UV-02) share a similar pattern with high hematite content, indicating a relatively dry sedimentary environment (i.e., aeolian

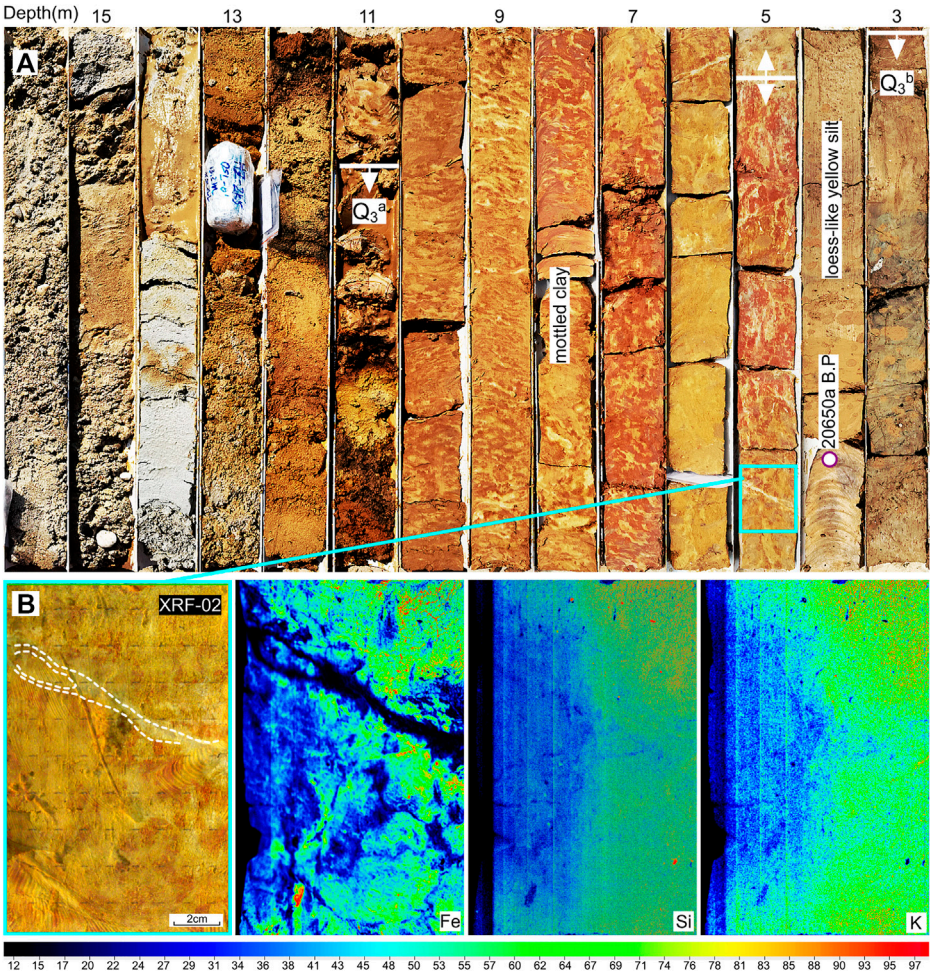

FIGURE 6
Photograph **(A)** and μ-XRF element mapping of mottled clay structure **(B)** of core HZ-ZK05. The sand vein is characterized by low Fe concentrations.

deposit). In contrary, samples of the white fraction of the mottled clay and fluvial sediment were predominantly goethite, reflecting a typical aquatic environment.

5 Discussion

5.1 Identification of the soft-sediment deformation structure

Mottled clay is primarily regarded as a weathering product of underlying fluvial/marine sediments (Huang, 1982; Li et al., 1984). Based on the evidences from grain size, mineral, and geochemical composition, Wang et al. (2018b) suggested no obvious weathering transition relationship between mottled clay and its underlying sediments, and proposed that the mottled structure was formed by post-sedimentary oxidation modification of homogeneous aeolian dust accumulated during the last glacial period, under the hot and humid conditions of the Holocene epoch. However, in the HZB, the mottled clay layer was not always overlaid with the Holocene organic-rich sediments. Instead, it is also overlaid with late Pleistocene fluvial sand (e.g., in core HZ-ZK12, Figure 7), or occurs as an interbed within the thick layer of homogeneous yellow silt (Figure 4A). Therefore, we suggest that the mottled clay is neither a post-sedimentary oxidation product of the loess-like yellow silt, nor a weathering product of the underlying fluvial/marine sediments. Alternatively, μ-XRF element mapping shows that the red/white fraction of mottled clay has a different geochemical composition (Figures 5–7). Two major components of grain size (5 and 80–90 μm) are identical to the modal sizes of the yellow silt and the underlying fluvial sand, respectively (Figure 4B). In addition, the red fraction of mottled clay had a high hematite content, similar to loess-like yellow silt, whereas the white fraction and the underlying fluvial sediments were dominated by goethite (Figure 8). These two types of iron oxides refer to opposite sedimentary environments (i.e., dry vs. wet conditions), implying that the accumulation of these two fractions was asynchronous. Furthermore, there are diverse deformed structures in the mottled clay, such as fragmented structures (Figure 5B), sand veins (Figure 6B), sand dykes (Figure 7B) and flame structure. The degree of deformation also increases upwards in mottled clay, which is a common characteristic of liquefaction-related

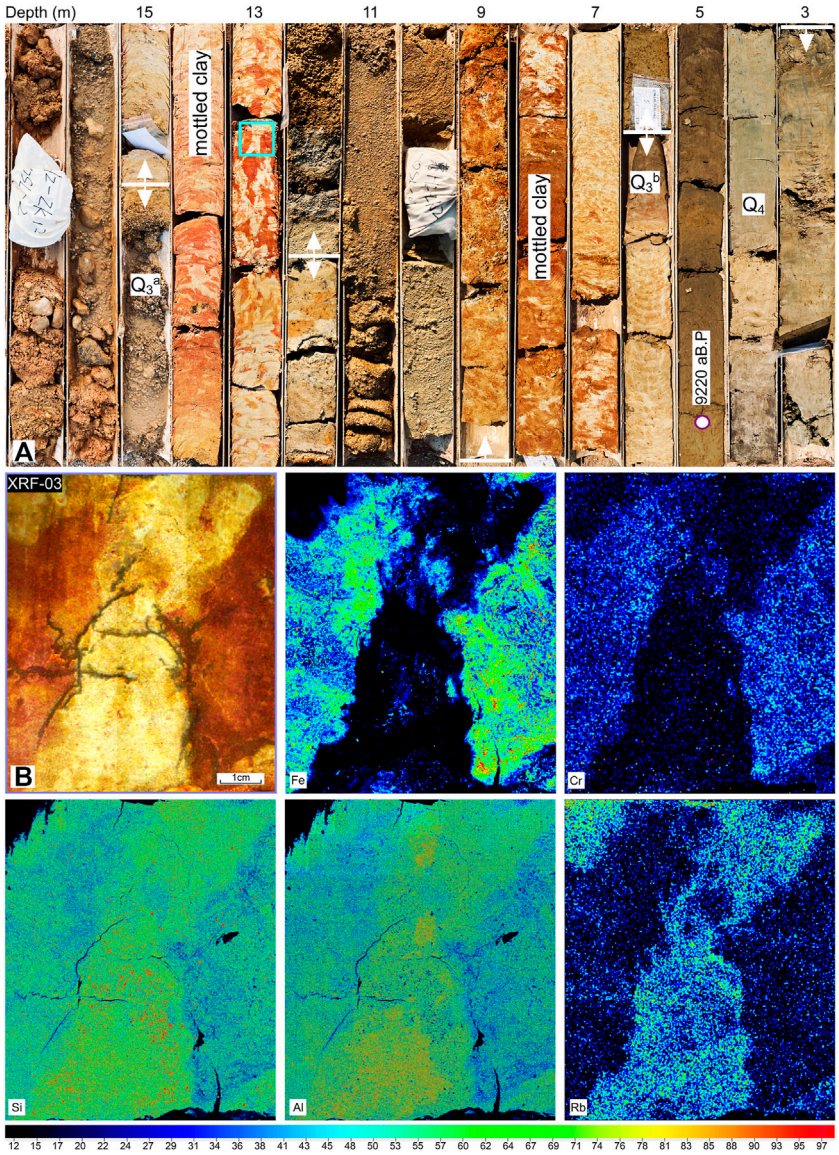

FIGURE 7
Photograph **(A)** and μ-XRF element mapping of mottled clay structure **(B)** of core HZ-ZK12.

deformations (Owen and Moretti, 2011). Therefore, we suggest that the mottled clay structure in the HZB is a product of liquefaction-induced SSD, which produced an admixture of aeolian yellow silt and underlying fluvial sand.

Several key factors of sediment characteristics, including grain size, porosity, saturation, permeability barrier, overburden pressure, and sediment history strongly influence susceptibility to liquefaction (Owen and Moretti, 2011). In most cases, liquefaction develops in loose, water-saturated silt or fine sand without previous liquefaction. A higher overburden pressure could also decrease the potential for liquefaction, such that most liquefaction develops in sediment with a small buried depth (generally less than 5 m) (Obermeier, 1996). In HZB, the underlying fluvial sand is mostly fine, loose, and water-saturated. In the other hand, the overlying yellow silt layer could act as a permeability barrier, leading to an increase in the pore-fluid pressure. These sedimentary characteristics of the HZB generally promote the development of liquefaction. Moreover, the fluvial sand and aeolian yellow silt are significantly different in many sedimentary characteristics, such as grain size, iron oxides, and geochemical (Figures 4–8), which favors the preservation of liquefaction-induced SSDS.

5.2 Triggers for the liquefaction and related SSDS

Liquefaction-induced SSDS can be triggered by many factors, which can be categorized into two types (Owen and Moretti, 2011). The first type is directly associated with sedimentation processes and termed autogenic or internal triggers and includes groundwater

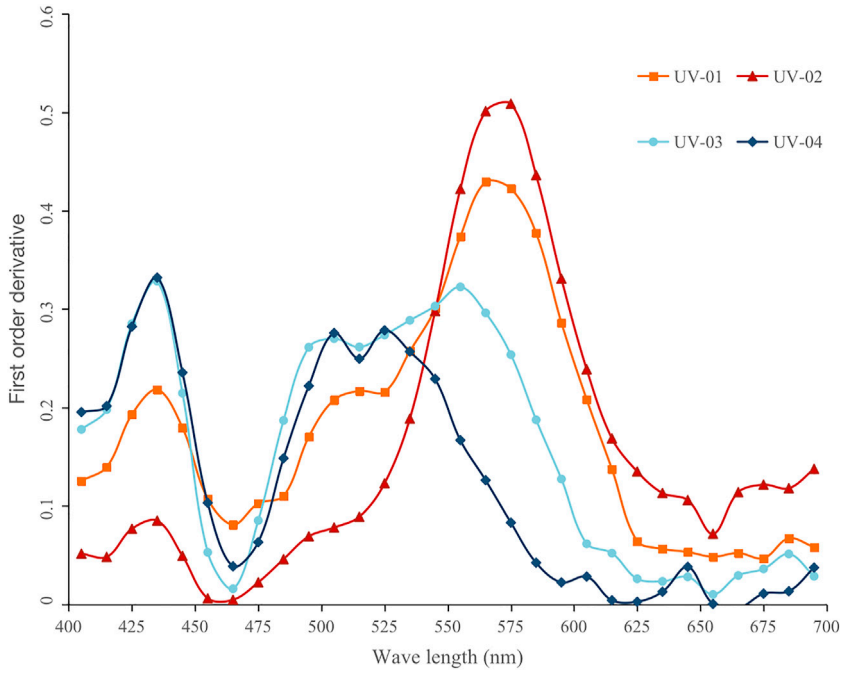

FIGURE 8
DRS first order derivative curves of different lithological samples in the Huizhou Basin. Samples of UV-01 to UV-04 refer to the loess-like yellow silt, the red fraction of mottled clay, the white fraction of mottled clay and fluvial sand, respectively.

fluctuations, water flows/waves, rapid sediment loading, tidal shear, tsunamis and permafrost thawing. Other triggers such as earthquakes, meteorite impacts and volcanic eruptions act as external agents (Su et al., 2022), and are referred to as allogenic triggers. Regarding the liquefaction-induced SSDS of mottled clay in the HZB, some triggers could be eliminated by exclusion. First, meteorite impacts and volcanic eruptions can be ruled out, because such events could produce unique geomorphological formations and sedimentary deposits, which have not been found in the study region since the late Pleistocene. The high hematite content in the red fraction of mottled clay indicates a relatively dry sedimentary environment, and in some cases, a mottled clay structure occurs interbedded with aeolian yellow silt (e.g., core HZ-ZK06), which together exclude an underwater sedimentary environment and thus possible triggers of water flows/waves and tidal shear. Third, the Lianhuashan Mountains situated between the HZB and the northern SCS (Figure 1B) could be a barrier weakening the influence of tsunamis and storm surges. Finally, paleotemperature reconstruction from a nearby maar lake indicates a drop of about 6 °C during the Last Glacial Maximum, a period of maximum glacier extent since the late Pleistocene, compared to modern annual temperature (Chu et al., 2017). Considering the present subtropical climate with hot conditions (e.g., 14.5 °C in winter) (Li et al., 2008), the freeze-thaw process was not likely the trigger that led to the formation of SSDS in the mottled clay layer of the HZB.

Instead, liquefaction-induced SSDS in the mottled clay layer of the HZB were interpreted as tectonic activity -induced after consideration of all other possible trigger agents. As a subsidence basin controlled by active faults (Figure 1B), the HZB has experienced tectonic activity since the late Pleistocene. For example, a normal fault cutting a peat bed dated at 33.59 ± 0.16 ka BP was found in the Huizhou fault zones (unpublished data). After homogeneous aeolian dust accumulation, seismic shaking led to a sudden increase in pore-water pressure and triggered the liquefaction of the underlying fluvial sediments. The excessive pore pressure water and sand mixture upwelled and intruded into the overlying loess-like yellow silt layer. This intrusion deformed the homogeneous aeolian layer, formed vertical structures (e.g., sand vein), and resulted in an admixture of aeolian silt and fluvial sand as revealed by the results of grain size, DRS and μ-XRF analysis. Moreover, the spatial distribution of the mottled clay layer is highly related to regional faults (Figure 9). For example, most cores with mottled clay layers were concentrated in the communicating zone of the Tonghu and Huizhou faults, where a historical earthquake with the magnitudes of 4 occurred in October 1590 (Wei et al., 2000). The spatial relationship between the mottled clay layers and regional faults strongly supports the suggestion of tectonic activity -induced liquefaction and SSDS. Notably, the formation of mottled clay structures in the different cores did not occur during a single seismic event. Generally, seismic events tend affect surface sediments (e.g., Shao et al., 2020). Multiple deformed layers in the vertical direction (e.g., two layers in core HZ-ZK12) reflect the repetition of paleo-earthquakes since the late Pleistocene in the HZB.

Seismically induced liquefaction and SSDS are usually recorded in lacustrine (e.g., Becker et al., 2002; Fan et al., 2022), fluvial (e.g., Suter et al., 2011; Rossetti et al., 2017) and aeolian (e.g., Moretti, 2000; Brand and Maithel, 2020) sediments. In the upper Senne area of Northwest Germany, seismically triggered SSDS in mixed alluvial

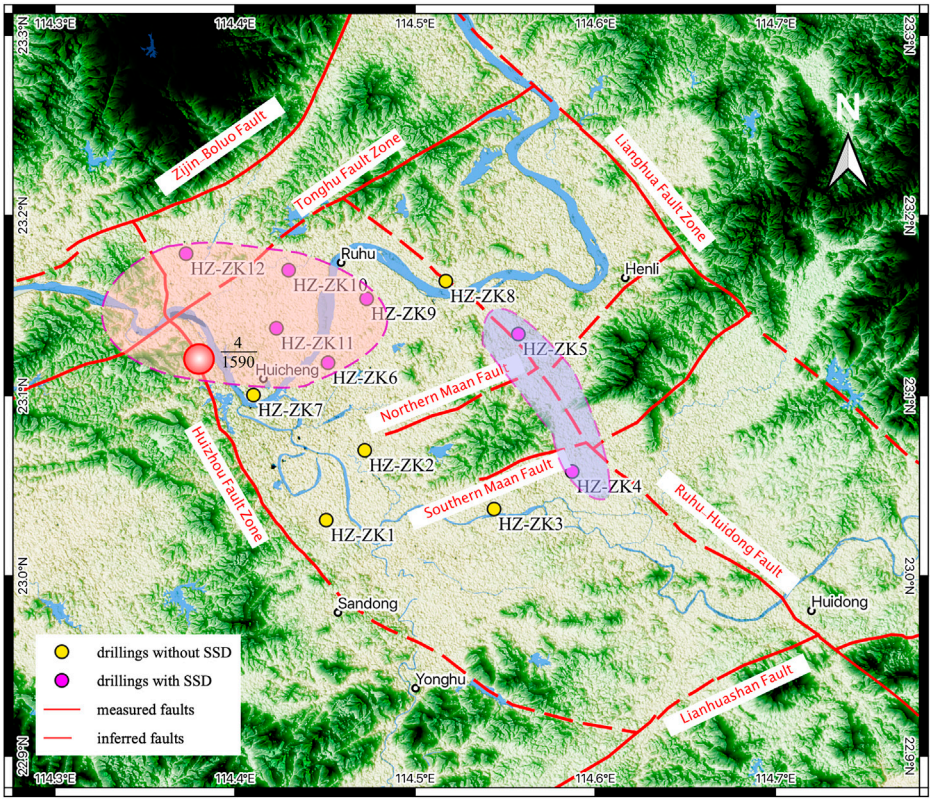

FIGURE 9
Spatial distribution of mottled clay layer in the Huizhou Basin. There is a close spatial relationship between mottled clay and regional faults.

and aeolian deposits that accumulated during the Last Glacial were also recognized (Brandes and Winsemann, 2013). Two outcrops from the Senne area consist mainly of alluvial deposits, overlain by several-meter-thick aeolian deposits, similar to the lithological succession of late Quaternary sediments in the HZB. Different types of SSDS, including closely spaced low offset normal faults, ball-and-pillow structures, flame structures, sills and irregular sedimentary intrusions, dikes, and sand volcanoes, were identified based on a detailed sedimentological analysis (Brandes and Winsemann, 2013). In the coastal region of the northern SCS, aeolian yellow silt broadly developed during the Last Glacial period in coastal basins, mostly underlain by late Pleistocene fluvial or alluvial deposits. This lithological succession is susceptible to seismically induced liquefaction. Therefore, the SSDS of the mottled clay layer could be a potential indicator of paleo-earthquakes in the coastal region of the northern SCS.

6 Conclusion

Tectonically induced liquefaction and the resulting SSDS are of great significance in long-term research on paleo-earthquakes in tectonically active regions. In this study, we combined age dating, grain size analysis, μ-XRF element mapping and DRS measurement to characterize the mottle clay structure in the HZB. The results indicate that mottle clay is an admixture of aeolian yellow silt and underlying fluvial sands, originating from liquefaction-induced SSDS during the late Pleistocene. After considering possible trigger agents, tectonic activity was considered to have trigger liquefaction and SSDS, which is supported by the close spatial relationship between mottled clay and regional faults. The SSDS of mottled clay could be a potential indicator of paleo-earthquakes in the coastal region of the northern South China Sea.

Data availability statement

The original contributions presented in the study are included in the article/Supplementary Material, further inquiries can be directed to the corresponding author.

Author contributions

ZC: Conceptualization, Methodology, Investigation, Writing–original draft, Writing–review and editing, Funding acquisition. WW: Methodology, Investigation, Writing–review and editing, Funding acquisition. PH: Methodology, Investigation, Writing–review and editing. YT: Methodology,

Investigation. JW: Methodology. QZ: Conceptualization, Methodology, Investigation, Writing–review and editing. CC: Conceptualization, Methodology, Investigation, Writing–original draft, Writing–review and editing, Funding acquisition.

Funding

This work was supported by the China Postdoctoral Science Foundation (Grant No. 2021M703659), 2021 Urban Geological Investigation of Huizhou City, Guangdong Province, China (Grant No. GDJR2021066), and Special Fund for Special Project of Geological Hazard Control, Guangdong Province, China (Grant No. 2017201).

Acknowledgments

The authors are grateful to Xibing Yang, Yuanxiao Huang, Huilin Niu and Jinlong Zhang from the Non-ferrous Metals Geological Bureau of Guangdong Province 935 Battalion for their assistance in the field.

Conflict of interest

The authors declare that the research was conducted in the absence of any commercial or financial relationships that could be construed as a potential conflict of interest.

Publisher's note

Supplementary material

The Supplementary Material for this article can be found online at: https://www.frontiersin.org/articles/10.3389/feart.2023.1135335/full#supplementary-material

References

Allen, J. R. L. (1986). Earthquake magnitude-frequency, epicentral distance, and soft-sediment deformation in sedimentary basins. *Sediment. Geol.* 46, 67–75. doi:10.1016/0037-0738(86)90006-0

Balsam, W., Ji, J. F., and Chen, J. (2004). Climatic interpretation of the Luochuan and Lingtai loess sections, China, based on changing iron oxide mineralogy and magnetic susceptibility. *Earth Planet. Sci. Lett.* 223, 335–348. doi:10.1016/j.epsl.2004.04.023

Becker, A., Davenport, C. A., and Giardini, D. (2002). Palaeoseismicity studies on end-Pleistocene and Holocene lake deposits around Basle, Switzerland. *Geophys. J. Int.* 149, 659–678. doi:10.1046/j.1365-246X.2002.01678.x

Brand, L., and Maithel, S. (2020). Small-scale soft-sediment deformation structures in the cross-bedded Coconino Sandstone (Permian; Arizona, United States); Possible evidence for seismic influence. *Front. Earth Sci.* 9, 723495. doi:10.3389/feart.2021.723495

Brandes, C., and Winsemann, J. (2013). Soft-sediment deformation structures in NW Germany caused by Late Pleistocene seismicity. *Int. J. Earth Sci.* 102, 2255–2274. doi:10.1007/s00531-013-0914-4

Bureau of Geology and Mineral Resources of Guangdong Province (BGMRGP) (1988). Regional Geology of Guangdong Province. Beijing: Geological Publishing House.

Chen, G. N., Zhang, K., Li, L. F., Shao, R. S., Zhuang, W. M., and Lin, X. M. (2002). Development of the Pearl River Delta in SE China and its relations to reactivation of basement faults. *J. Geosci. China* 14 (1), 17–24.

Chu, G. Q., Sun, Q., Zhu, Q. Z., Shan, Y. B., Shang, W. Y., Ling, Y., et al. (2017). The role of the Asian winter monsoon in the rapid propagation of abrupt climate changes during the last deglaciation. *Quat. Sci. Rev.* 177, 120–129. doi:10.1016/j.quascirev.2017.10.014

Cornell, R. M., and Schwertmann, U. (2003). *The iron oxides: Structure, properties, reactions, occurrences, and uses*. Weinheim: Wiley VCH.

Deaton, B. C., and Balsam, W. L. (1991). Visible spectroscopy: A rapid method for determining hematite and goethite concentration in geological materials. *J. Sediment. Petrol.* 61, 628–632. doi:10.1306/D4267794-2B26-11D7-8648000102C1865D

Deev, E. V., Zolnikov, I. D., and Gus'kov, S. A. (2009). Seismites in quaternary sediments of southeastern altai. *Russ. Geol. Geophys.* 50 (6), 546–561. doi:10.1016/j.rgg.2008.10.004

Fan, J. W., Xu, H. Y., Shi, W., Guo, Q. Q., Zhang, S. Q., Wei, X. T., et al. (2022). A ~28-kyr continuous lacustrine paleoseismic record of the intraplate, slow-slipping Fuyun Fault in Northwest China. *Front. Earth Sci.* 10, 828801. doi:10.3389/feart.2022.828801

Galli, P. (2000). New empirical relationships between magnitude and distance for liquefaction. *Tectonophysics* 324, 169–187. doi:10.1016/S0040-1951(00)00118-9

Gladkov, A. S., Lobova, E. U., Deev, E. V., Korzhenkov, A. M., Mazeika, J. V., Abdieva, S. V., et al. (2016). Earthquake-induced soft-sediment deformation structures in Late Pleistocene lacustrine deposits of Issyk-Kul lake (Kyrgyzstan). *Sediment. Geol.* 344, 112–122. doi:10.1016/j.sedgeo.2016.06.019

Hibsch, C., Alvarado, A., Yepes, H., Perez, V. H., and Sébrier, M. (1997). Holocene liquefaction and soft-sediment deformation in quito (Ecuador): A paleoseismic history recorded in lacustrine sediments. *J. Geodyn.* 24, 259–280. doi:10.1016/S0264-3707(97)00010-0

Hoehnel, D., Reimold, W. U., Altenberger, U., Hofmann, A., Mohr-Westheide, T., Özdemir, S., et al. (2018). Petrographic and Micro-XRF analysis of multiple archean impact-derived spherule layers in drill core CT3 from the northern Barberton Greenstone Belt (South Africa). *J. Afr. Earth Sci.* 138, 264–288. doi:10.1016/j.jafrearsci.2017.11.020

Huang, Z. G. (1982). *Formation and evolution of the Pearl River Delta of China*. Guangzhou Branch, Guangzhou: Popular Science Press.

Ji, J. F., Balsam, W., Chen, J., and Liu, L. W. (2002). Rapid and quantitative measurement of hematite and goethite in the Chinese loess-paleosol sequence by diffuse reflectance spectroscopy. *Clay Clay Min.* 50, 208–216. doi:10.1346/000986002760832801

Li, P. R., Huang, G., Zhang, Z. Y., and Li, K. H. (1984). Quaternary stratigraphy in the zhujiang delta. *Sci. Geogr. Sin.* 4 (2), 133–142.

Li, M. H., Cui, S. P., Wu, N. K., Zhang, Z. F., Fan, S. J., and Yang, L. (2008). The characteristics of temperature change of Huizhou in the past half century. *J. Trop. Meteorol.* 24 (4), 435–440.

Li, J. H., Cawood, P. A., Ratschbacher, L., Zhang, Y. Q., Dong, S. W., Xin, Y. J., et al. (2020). Building Southeast China in the late Mesozoic: Insights from alternating episodes of shortening and extension along the Lianhuashan fault zone. *Earth-Sci. Rev.* 201, 103056. doi:10.1016/j.earscirev.2019.103056

Li, Y. H., Guo, L. T., and Yan, Y. X. (2021). Earthquake hazard evaluation of Huizhou fault and its adjacent area. *Seismol. Geomagn. Obs. Res.* 42 (1), 48–60. doi:10.3969/j.issn.1003-3246.2021.01.008

Liang, L. J., Dai, F. C., Jiang, H. C., and Zhong, N. (2018). A preliminary study on the soft-sediment deformation structures in the late Quaternary lacustrine sediments at Tashkorgan, northeastern Pamir, China. *Acta Geol. sin.-engl. Ed.* 92 (4), 1574–1591. doi:10.1111/1755-6724.13644

Moretti, M. (2000). Soft-sediment deformation structures interpreted as seismites in middle-late Pleistocene aeolian deposits (Apulian foreland, southern Italy). *Sediment. Geol.* 135, 167–179. doi:10.1016/S0037-0738(00)00070-1

Obermeier, S. F. (1996). Use of liquefaction-induced features for paleoseismic analysis — an overview of how seismic liquefaction features can be distinguished from other features and how their regional distribution and properties of source sediment can be used to infer the location and strength of Holocene paleo-earthquakes. *Eng. Geol.* 44, 1–76. doi:10.1016/S0013-7952(96)00040-3

Owen, G., and Moretti, M. (2011). Identifying triggers for liquefaction-induced soft-sediment deformation in sands. *Sediment. Geol.* 235, 141–147. doi:10.1016/j.sedgeo.2010.10.003

Qiao, X. F., Li, H. B., Su, D. C., He, B. Z., Tian, H. S., Guo, X. P., et al. (2017). *Soft-sediment deformation structures*. Beijing: Geological Publishing House.

Reimer, P. J., Austin, W. E. N., Bard, E., Bayliss, A., Blackwell, P. G., Bronk Ramsey, C., et al. (2020). The IntCal20 Northern Hemisphere radiocarbon age calibration curve (0-55 cal kBP). *Radiocarbon* 62, 725–757. doi:10.1017/RDC.2020.41

Rossetti, D. F., Alves, F. C., and Valeriano, M. M. (2017). A tectonically-triggered late Holocene seismite in the southern Amazonian lowlands, Brazil. *Braz. Sediment. Geol.* 358, 70–83. doi:10.1016/j.sedgeo.2017.07.003

Shao, Z. F., Zhong, J. H., Howell, J., Hao, B., Luan, X. W., Liu, Z. X., et al. (2020). Liquefaction structures induced by the M5.7 earthquake on May 28, 2018 in Songyuan, Jilin Province, NE China and research implication. *J. Palaegeogr.* 9, 3. doi:10.1186/s42501-019-0053-3

Song, F. M., Wang, Y. P., Li, C. Y., Chen, W. G., and Zhao, H. M. (2001). New insight into the Quaternary activity of Wuguishan southern piedmont fault in Zhujiang Delta. *Seismol. Geol.* 23 (4), 521–526.

Su, D. C., Sun, A. P., Li, Z. L., Chen, S. Y., and Wu, Z. J. (2022). Origin of soft-sediment deformation structures in Nihewan Basin. *J. Palaegeogr.* 11 (3), 332–359. doi:10.1016/j.jop.2022.05.002

Sun, Y. B., He, L., Liang, L. J., and An, Z. S. (2011). Changing color of Chinese loess: Geochemical constraint and paleoclimatic significance. *J. Asian Earth Sci.* 40, 1131–1138. doi:10.1016/j.jseaes.2010.08.006

Suter, F., Martínez, J. I., and Vélez, M. I. (2011). Holocene soft-sediment deformation of the Santa Fe-Sopetrán Basin, northern Colombian Andes: Evidence for pre-Hispanic seismic activity? *Sediment. Geol.* 235, 188–199. doi:10.1016/j.sedgeo.2010.09.018

Tang, Y. K., Chen, G. N., Peng, Z. L., and Zhang, K. (2011). Late quaternary tectonics of the Pearl River Delta, SE China: Evidence from Xilingang. *Geodin. Acta* 24 (3-4), 133–139. doi:10.3166/ga.24.133-139

Tang, Y. J., Zheng, Z., Chen, C., Wang, M. Y., and Chen, B. S. (2018). Evolution of the Lian River coastal basin in response to Quaternary marine transgressions in Southeast China. *Sediment. Geol.* 366, 1–13. doi:10.1016/j.sedgeo.2018.01.003

Tuttle, M. P., Wolf, L., Hartleb, R., and Mayne, P. W. (2019). Paleoliquefaction studies and the evaluation of seismic hazard. *Geosciences* 9 (7), 311. doi:10.3390/geosciences9070311

Üner, S., Özsayın, E., and Selçuk, A. S. (2019). Seismites as an indicator for determination of earthquake recurrence interval: A case study from erciş fault (eastern anatolia-Turkey). *Tectonophysics* 766, 167–178. doi:10.1016/j.tecto.2019.06.010

Wang, J., Chen, Z., Gao, Q. Z., Grapes, R., Peng, Z. L., and Chen, G. N. (2018a). Late Pleistocene loess-like deposits in the coastal area of south China. *Catena* 167, 305–318. doi:10.1016/j.catena.2018.04.032

Wang, J., Chen, Z., Gao, Q. Z., and Chen, G. N. (2018b). New research on the origin of mottled clay in Quaternary basins in the coastal area of south China. *Aeolian Res.* 32, 170–180. doi:10.1016/j.aeolia.2018.02.006

Wei, B. L., Chen, R. F., and Huang, R. H. (2000). *Seismotectonic map of Guangdong Province*. Beijing: Seismological Press.

Xu, X., He, C. H., and Shen, Z. D. (1992). *Research methods of quaternary environment*. Guiyang: Guizhou Science and Technology Press.

Yao, Y. T., Zhan, W. H., Liu, Z. F., Zhang, Z. Q., Zhan, M. Z., and Sun, J. (2013). Neotectonics and its relations to the evolution of the Pearl River Delta, Guangdong, China. *J. Coast. Res.* 66 (1), 1–11. doi:10.2112/SI_66_1

Zhang, W. G., Yu, L. Z., Zheng, L. M., Ji, X. M., Zhou, J. F., Wang, L. M., et al. (2009). East Asian summer monsoon intensity inferred from iron oxide mineralogy in the Xiashu Loess in southern China. *Quat. Sci. Rev.* 28, 345–353. doi:10.1016/j.quascirev.2008.10.002

Zhong, N., Jiang, H. C., Li, H. B., Su, D. C., Xu, H. Y., Liang, L. J., et al. (2022). The potential of using soft-sediment deformation structures for quantitatively reconstructing paleo-seismic shaking intensity: Progress and prospect. *Environ. Earth Sci.* 81, 408. doi:10.1007/s12665-022-10504-8